SUPPLEMENTARY MATERIAL

In the following, we give further details on the new algorithms presented in this paper and outlined in Figure S1, and discuss the methods used for spectral analysis of time series of F-actin turnover. To facilitate the association with the main text, section titles in the supplementary material correspond to those in the paper.

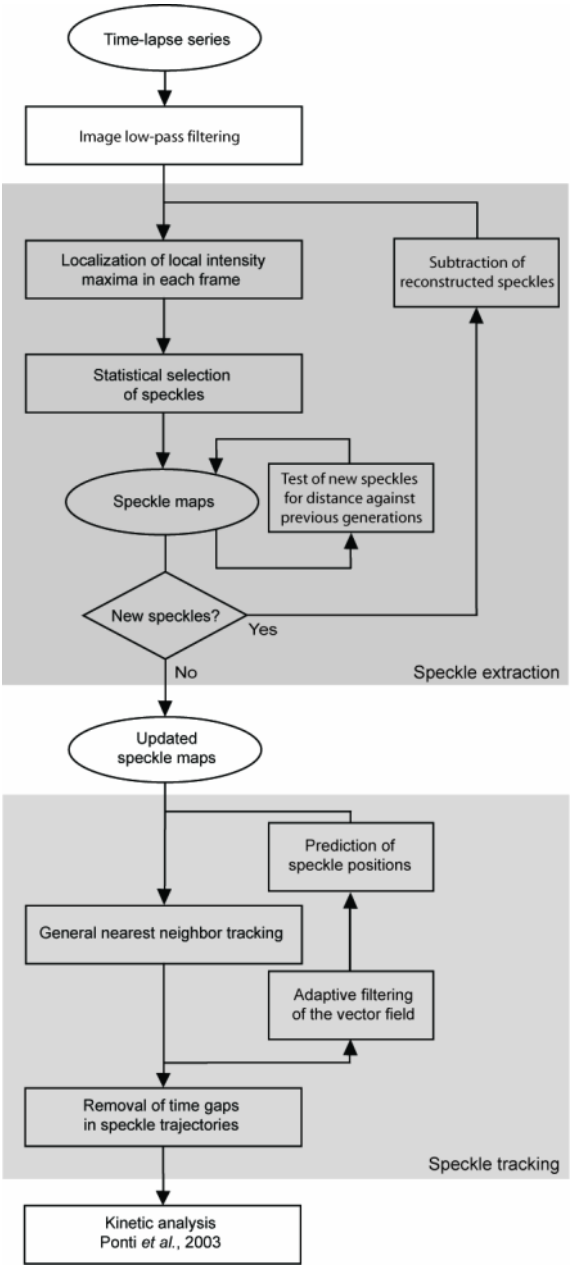

Figure S1: Flow chart of Fluorescent Speckle Microscopy (FSM) data analysis. Shaded boxes indicate modules with major modifications to the analysis framework described in (1). Iterative speckle extraction is applied to retrieve the significant number of speckles in clusters with substantial signal overlaps. Speckle tracking relies on iterative prediction of speckle positions.

ANALYSIS OF FLUORESCENT SPECKLES

Iterative speckle extraction

Speckle fusions induced by low-pass filtering and local maximum detection

To determine the extent to which speckle proximity and signal-to-noise ratio (SNR) contribute to speckle fusions in a discrete image space, we performed Monte Carlo simulations counting the number of repeats where the local maximum operator successfully detected two proximate speckles. The two speckles were modeled as two-dimensional Gaussian intensity distributions with a relative intensity ratio $A = I_1 / I_2$ and separated by a distance r. The distance r was limited to values greater than the Sparrow criterion (2), i.e. under-noise free conditions and in a continuous image space, the two Gaussians produce two local maxima. For $A = 1.0$, the Sparrow criterion amounts to 3.2 pixels for a $N.A. = 1.4$, 100 X objective lens, and 6.7 μm pixel size. With $A = 2.0$, the value increases to 4.20 pixels. To simulate specific SNR conditions, we added normally-distributed noise values to the synthetic speckle signals. This signal was then subjected to low-pass filtering followed by local maximum detection.

We analyzed the detection performance for the parameter ranges $1 < A < 3$, $4.0 < r < 5.5$ pixels and four SNR values: ∞, 10, 7, and 4. Fig S2a displays the success rate for an example with A = 1.5. The rate was defined as the number of Monte Carlo runs in which the local maximum operator detected two speckles divided by the total number of runs. With $\mathrm{SNR} = \infty$, two speckles of a certain intensity ratio are indistinguishable below a distance r_0. Notice that because of the intensity difference, the finite support of the low-pass filter and the finite resolution of the local maximum operator, r_0 is greater than the Sparrow criterion. In the following we refer to $r_0(A)$ as the *generalized Sparrow criterion* (*GSC*). If two speckles are detected at a distance $r < r_0$, at least one of them will represent a spurious, noise-induced speckle. The lower the SNR the higher is the number of speckles falsely detected below the GSC (Fig. S2*a*). Importantly, for distances $r > r_0$, the local maximum operator still fails to consistently detect both speckles. Those speckles have hitherto been lost by our detector but are now recovered by iterative speckle extraction (ISE).

We also examined the success rate of the local maximum operator as a function of the intensity ratio A (Fig. S2*b*; for a fixed distance $r = 4.6$ pixels). The curve with $\mathrm{SNR} = \infty$ indicates the inverse of the GSC A_{crit} for $r = r_0 = 4.6$ pixels . For ratios $A > A_{crit}$ noise causes the detection of spurious speckles, while true speckles are missed in the range $1 < A < A_{crit}$.

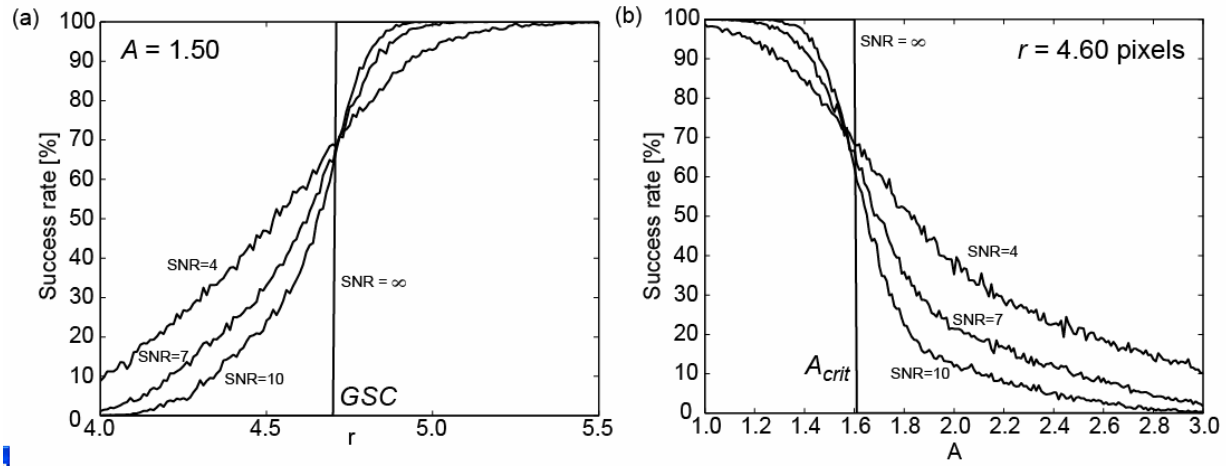

Figure S2: Success rate of the local maximum operator in detecting two proximate speckles after low-pass filtering. The success rate is a function of the signal-to-noise ratio (SNR) and the distance *r* **(*a*)**; as well as the intensity ratio *A* between the speckles **(*b*)**. Curves with SNR = ∞ define the generalized Sparrow criterion (*GSC*) and the critical intensity ratio A_{crit} for detecting a true secondary speckle proximate to a primary speckle. Detection of a second local maximum below the GSC or larger than A_{crit} is caused by image noise. The two limits are interdependent.

Recovery of higher-order speckles to resolve fused speckles

Some of the higher-order speckles are artifacts generated by the image subtraction. They violate the GSC. To exclude those, we test in any iteration if the distance of all newly extracted, higher-order speckles to any speckle extracted and accepted in previous iterations exceeds the GSC. To derive the GSC for two speckles at distance *r*, we consider the peak intensity ratio $A = \Delta I_1 / \Delta I_2$, with $\Delta I_{1/2} = I_{1/2} - I_B$ denoting the difference between the peak intensities $I_{1/2}$ and a common background I_B . For low signal-to-noise ratio (SNR) conditions, the PSF can be approximated by a Gaussian with standard deviation $s = 0.21\,\lambda/\mathrm{N.A.}$ (3). λ and N.A. denote the emission wavelength of the fluorophore and the numerical aperture of the optics, respectively. For a coordinate system centered on the first speckle, the normalized intensity profile along the axis connecting the two speckles can thus be written as

$$\tilde{I}(x) = \left(I_1(x) + I_2(x) - I_B\right)/\Delta I_2 = Ae^{-\frac{1}{2}\frac{x^2}{s^2}} + e^{-\frac{1}{2}\frac{(x-r)^2}{s^2}}. \qquad \text{(S1)}$$

Fig. S3a depicts the function for $A = 1.5$ and the three cases $r > r_0$, $r < r_0$ and $r = r_0$ where $r_0 \approx 3.9$ pixels denotes the GSC for the imaging setup used in our experiments. Eq. S1 has a second-order extremum $\tilde{I}(x)' = \tilde{I}(x)'' = 0$ only when $r = r_0$, defining a unique relationship between the critical intensity ratio A_{crit} and the GSC r_0:

$$A_{crit} = \frac{r_0 - \omega}{r_0 + \omega} \cdot e^{\left(\frac{\omega r_0}{2s^2}\right)}, \text{ with } \omega = \sqrt{r_0^2 - 4s^2}\,. \qquad \text{(S2)}$$

Fig. S3b shows the inverse of Eq. S2. We utilize Eq. S2 to eliminate spurious higher-order speckles as follows: after computation of the critical intensity ratio $A_{ij,crit}(r_{ij})$ between newly extracted speckles $j = 1,...,N_S$ and all speckles from previous iterations $i = 1,...,N_{j,P}$ falling into a circular search area of radius $r_{\max} = 5.5$ pixels, we test if any ratio $A_{ij} = \Delta I_i / \Delta I_j$ is greater than $A_{ij,crit}$. If the test is passed the higher-order speckle *j* is rejected.

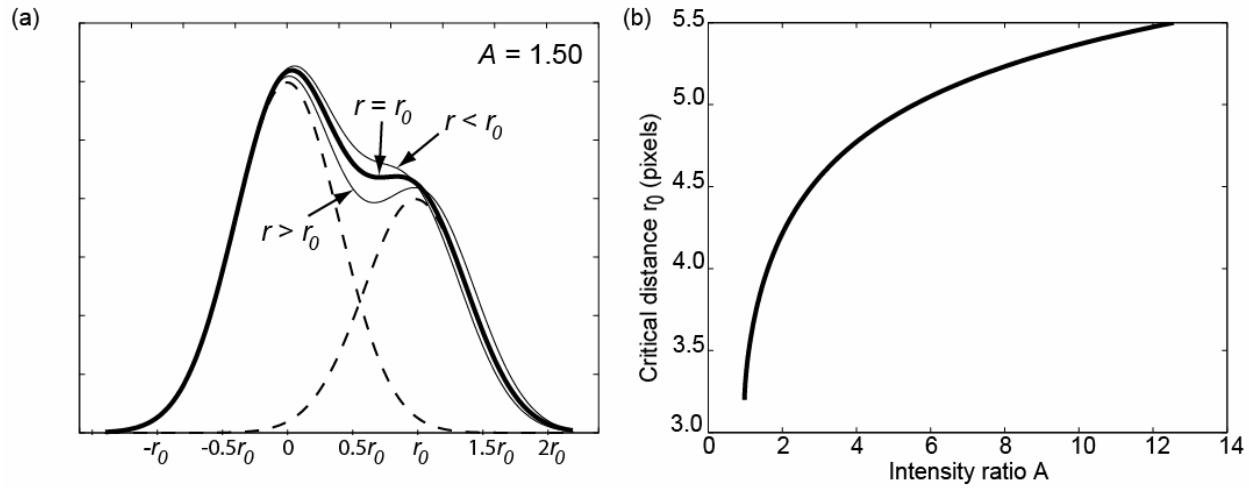

Figure S3: Theoretical limits in separation of overlapping speckles. (a) Illustration of the superposition of two diffraction-limited 1D signals beyond ($r > r_0$), below ($r < r_0$), and at the generalized Sparrow criterion ($r = r_0$) for the intensity ratio A = 1.5. (b) Definition of $r_0(A)$ (inverse of Eq. S2). See text for an explanation of how Eq. S2 is used to discriminate spurious local maxima from true overlapping speckles.

General nearest-neighbor (GNN) tracking with motion propagation

Enhanced speckle tracking by GNN and locally adaptive flow filtering

Fig. S4*a* illustrates the solution of global nearest neighbor tracking (Eq. 1, main text) for a simulated flow field with the characteristics $0.5\times\overline{r} < d < \overline{r}$ ($d = 3.6 \pm 0.6; \overline{r} = 5.4 \pm 0.42$, arbitrary units). As explained in the Algorithm section of the main text, for this configuration simple nearest neighbor tracking fails, even when executed with a global assignment for the resolution of topological conflicts. For the data shown here, the success rate of global nearest neighbor tracking reached 46% (number of correct links divided by number of simulated links). With GNN (Fig. S4*b*), the rate increases to 100%. The parameters for flow field simulation were set to be twice as hard as the most challenging conditions found experimentally in F-actin flow fields ($d = 1.9$ pixels/frame; $\overline{r} = 5.4 \pm 1.23$; corresponding to a flow speed of 1.5 μm/min).

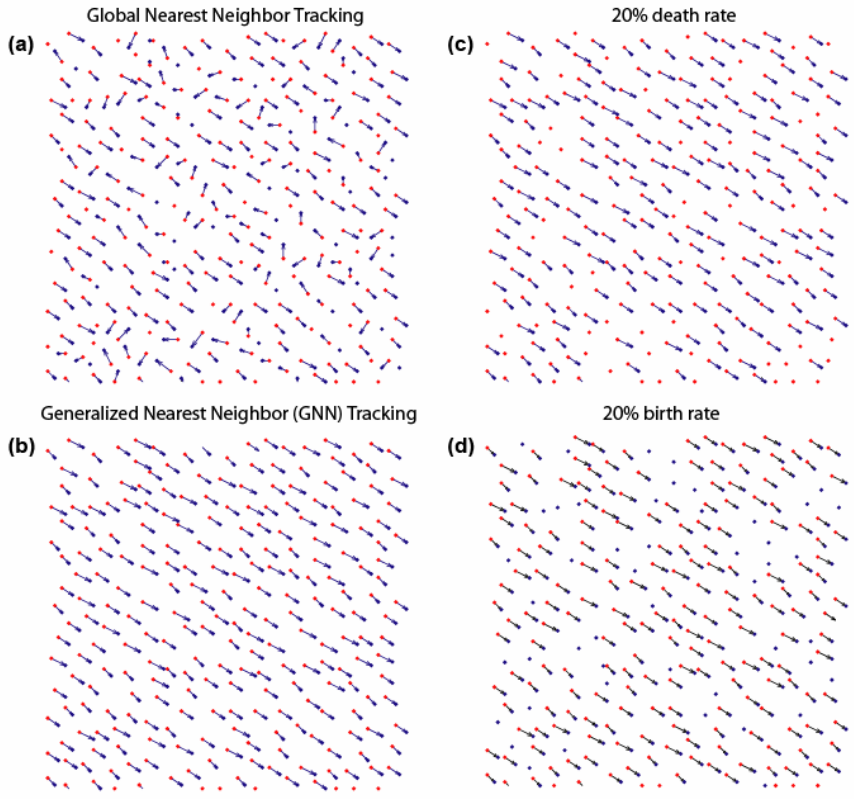

Figure S4: Performance enhancement in tracking locally coherent speckle flow by Generalized Nearest Neighbor (GNN) assignment. The flow field was simulated to match the characteristics of the experimental flow fields. **(*a*)** Speckle assignments by a global nearest neighbor method. **(*b*)** Speckle assignment by a GNN method using predicted speckle motion between frames. **(*c*–*d*)** GNN methods deliver 100% correct assignments also under the perturbation of 20% birth and death events.

The success rate stays 100% even when 20% of the speckles disappear (Fig. S4*c*) or 20% speckles are added (Fig. S4*d*). These birth and death rates correspond to an average lifetime of 5 frames (25 s) which is at least twice the rate observed in real experiments (shortest lifetimes amount to ~50 s, cf. Table S1). We can thus assume that in qFSM experiments GNN tracking is a minimal error source in trajectory reconstruction.

This conclusion implies that GNN tracking is supported by an error-free motion model for the prediction of speckle positions between frames. The motion model is derived by iterative filtering of speckle tracks (cf. main text). With the coherent flow field assumed in the simulations of Fig. S4*a-d*, this was straightforward to achieve, but the filtering can become difficult in experiments with strong flow gradients. We investigated the performance of locally adaptive flow filtering in presence of a flow gradient and shear flow (Fig. S5). Whereas the reconstruction of shear flow fields greatly improved with the proposed adaptive filtering, the reconstruction of flow fields with gradients in the direction of flow (acceleration or slow down) was not optimal. However, for the purpose of predicting speckle motion this turned out to be less critical, as over- or underestimation of the speckle displacements in the gradient direction were generally corrected by the GNN speckle assignment.

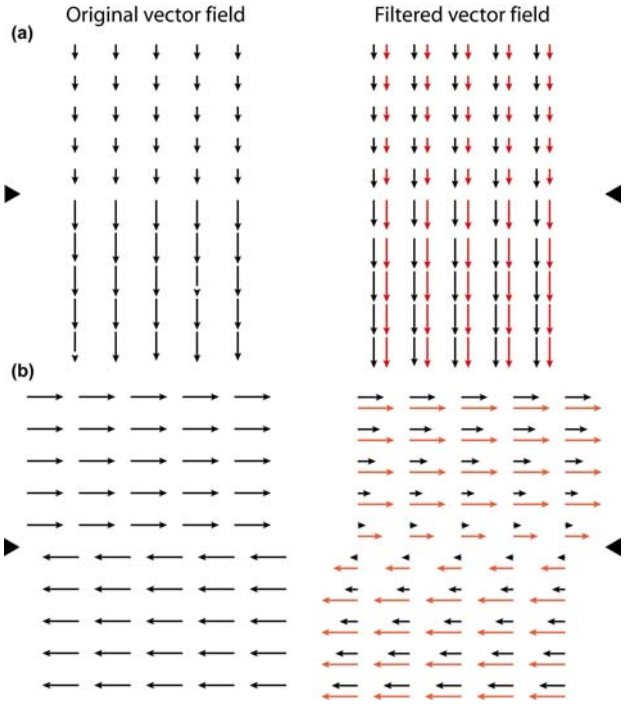

Fig. S5: Validation of gradient preserving vector filtering. **(*a*)** Left: simulated vector field with a gradient 1:3 in the direction of the flow field. Right: comparison of standard isotropic filtering (black) and adaptive, gradient-preserving filtering (red). **(*b*)** Left: simulated vector field with a shear gradient. Right: comparison of standard isotropic filtering (black) and adaptive, gradient-preserving filtering (red). Here, the second method markedly outperforms isotropic filtering.

Validation of speckle extraction and tracking on living cells

We also tested the performance of ISE and GNN tracking on live cell data. The results were presented in great detail in (4). Here, we summarize our finds as they relate to the improvement of speckle tracking and identification of birth and death events for the study of dynamic patterns of F-actin turnover.

First, we investigated how the image signal evolved throughout ISE. Time-lapse sequences of the residual images display the remarkable reduction of speckle flow with every iteration, demonstrating that the extracted speckles contain significant information of the network movement indeed (cf. Movie 2). After two or three iterations the residual images converged to a blurred signal with no further speckles to be detected.

Next, we investigated how the speckle lifetime and the amounts of birth and death events with significant kinetic scores depended on the application of ISE and GNN tracking (Table S1). Both statistics served as measures of the completeness of trajectories and hence of the accuracy of the kinetic scores derived from intensity changes at trajectory endpoints. As expected, in all experiments the enhanced algorithms yielded longer speckle lifetimes. Interesting differences were observed for ISE and GNN contributions to lifetime extension with different cell models. Whereas in contact-inhibited cells (C) or cells with slow flow (M1 and M2) most of the lifetime extension was achieved by ISE, the lifetime increase in more rapid flow fields (M3) depended on GNN tracking. In contact-inhibited cells the number of events, i.e. trajectory ends, was substantially reduced by ISE, as higher-order speckles filled in false gaps in the trajectories of primary speckles. Quite unexpected, however, in migrating cells (M1 – M3) the application of ISE increased the number of birth and death events. The application of GNN tracking slightly reduced this number but the total effect of both algorithms was an addition of trajectory ends. This means that higher-order speckles happen to generate a number of statistically significant trajectories that never include a primary speckle. These trajectories were missed completely in previous qFSM analyses (1), changing the maps of F-actin turnover in important details (Fig. 1*c-d*, main text). In line with this find was that ISE largely neutralized the integration of *ghost speckles* (speckles with a lifetime of only one frame, which are excluded from the kinetic analysis) into longer trajectories by adding new, higher-order ghost speckles (data shown in (4)). Therefore, as concluded in (1), ghost speckles are not an artifact caused by insufficient detection or tracking, but reflect fast mechanisms of F-actin turnover that are currently not captured by frame rates of 5 – 10 s.

The last row of Table S1 summarizes the joint effect of extended lifetime and additional high-order speckle trajectories. To distinguish between true and false speckle births and deaths, i.e. between events associated with local monomer exchange and those due to noise, speckle losses and creations related to in- and out-of-focus movements, and due to spontaneous

accumulation of fluorophore clusters by filament fluctuations, the algorithm runs several statistical tests on the foreground and background intensity changes at the time point of appearance and disappearance (1). Only if all tests are passed at a user-defined confidence level, a kinetic score will be assigned to the event. Ultimately, the spatial and temporal density of these scores determines the resolution of the turnover maps. Together, the algorithmic extensions discussed in this paper increase the density of scores by 5 – 25 %.

	C			**M1**			**M2**			**M3**		
	v = 75 nm/min			v = 290 nm/min			v = 210 nm/min			v = 460 nm/min		
	OE+NN	ISE	ISE+ GNN	OE+NN	ISE	ISE+ GNN	OE+NN	ISE	ISE+ GNN	OE+NN	ISE	ISE+ GNN
Lifetime (s)	**81.7**	**86.1** +5.5%	**86.2** +0.2% +5.6%	**62.2**	**68.6** +10.3%	**70.0** +2.1% +12.7%	**61.6**	**65.7** +6.6%	**66.5** +1.3% +7.9%	**65.4**	**67.3** +2.9%	**78.5** +16.5% +20.0%
				Lamellipodium		**68.1**			**51.2**			**50.8**
				Lamella		**80.1**			**71.8**			**88.7**
Number of events	**357915**	**289774** -19.0%	**287522** -0.8% -19.7%	**140794**	**156521** +11.2%	**153227** -2.1% +8.8%	**160270**	**189883** +18.5%	**184823** -2.7% +15.3%	**103291**	**123498** +19.6%	**107043** -13.3% +3.6%
Number of scores	**62669**	**66141** +5.0%	**65989** -0.2% +4.8%	**35676**	**43893** +23.0%	**42707** -2.7% +19.7%	**34320**	**43235** +25.7%	**42484** -1.5% +23.8%	**26545**	**34203** +28.9%	**30520** -10.8% +15.0%

Table S1: Increase in speckle lifetime and number of births and death events with significant scores due to iterative speckle extraction (ISE) and generalized nearest-neighbor tracking with propagation of speckle motion (GNN), as compared to ordinary extraction and nearest-neighbor tracking (OE+NN) described in (3). Data is presented from a contact-inhibited cell (C) with a spatially stationary F-actin network, and from migrating cells (M1 – M3) with F-actin networks undergoing retrograde flow. Also, for M1 – M3 average lifetimes for lamellipodium and lamella are distinguished.

RESULTS AND DISCUSSION

Periodic patterns of La turnover are composed of a limited set of characteristic frequencies

We studied the temporal evolution of F-actin turnover in the La by integrating kinetic scores in probing windows of 1.2 μm x 1.2. The windows followed the local retrograde flow of the network. We found local oscillatory behavior of assembly and disassembly (cf. main text).

To investigate whether these oscillations displayed characteristic frequencies, we performed spectral analysis of the time series. Our movies were acquired over 600 – 1000 s before the speckles bleached. With a turnover periodicity of ~60 – 200 s (Fig. 5d-f) the finite time series of one window thus captured between 3 – 16 full periods. The number of significant birth and death events contributing to the kinetic score of a window amounted to 2 – 4 per time point. Therefore, at this high spatial resolution the noise level in the raw time series was very high and it was questionable if only a few observed full periods would allow robust spectral decomposition by Fourier Transformation.

To answer this question, we simulated time series with a characteristic similar to the experimental data. We started with the superposition of four noise-free sine waves with periods of 34, 72, 97, and 114 s and same amplitude, sampled with 10 s sampling time over a period of 600 s (Fig. S6 *a*I). Spectral analysis of this signal recovered only three of the four frequencies. They were contaminated by large errors (Fig. S6 *a*II), indicating that the information from one probing window is not sufficient to decompose the oscillatory behavior of the signal. We therefore generated a 10-times longer signal, simulating the concatenation of time series from 10 probing windows. The analysis returned a satisfactory approximation of the real values (Fig. S6 *a*III). By extending the number of probing windows to 100 the four input frequencies were retrieved error-free (Fig. S6 *a*IV).

We continued the analysis in Figure 4S*b* by adding normally distributed noise to the time series (SNR=1). Both 1 (Fig. S6 *b*II), and 10 windows (Fig. S6 *b*III) were not sufficient for reconstruction of the spectral characteristics. The spectra were contaminated by numerous side peaks with a magnitude greater than the one of the weakest frequency in the series (34 s). Even with 100 windows (Fig. S6 *b*IV) the spectra had a substantial noise floor. Together these tests indicated that averaging of at least 100 windows was required to warranty the recovery of a mixture of different frequencies from a signal with SNR = 1.

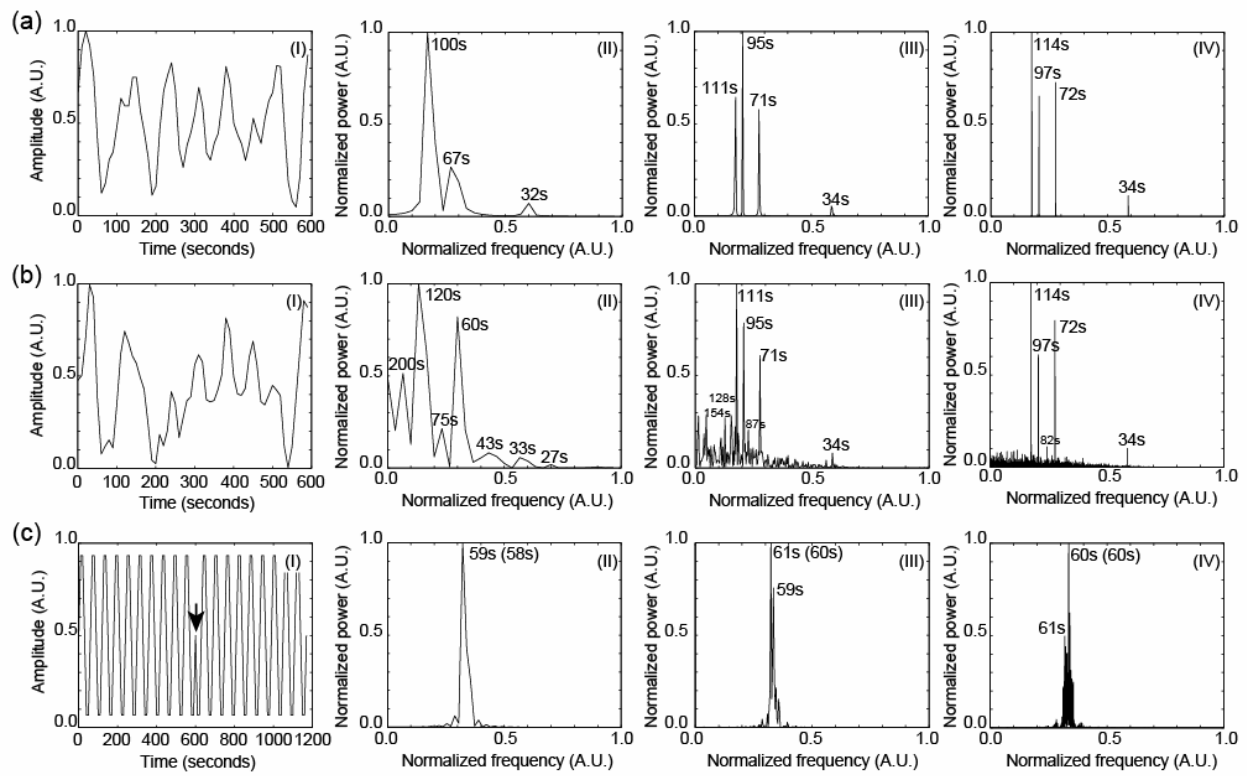

Figure S6: Spectral analysis of noisy sine wave mixtures sampled in sequences of 600 s at a rate of 10 s / frame. (***a*-I**) Superposition of four sine waves with periods of 34, 72, 97 and 114 s. These parameters were selected in agreement with the conditions observed in experimental data. (***a*-II**) Power spectrum retrieved from 1 window. The three peaks were associated with a period of 32 s and its two lower harmonics 67 and 100 s. (***a*-III**) Increasing the sampling period to 6000 s by concatenation of 10 sequences reduced the estimation error in the recovered spectra. (***a*-IV**) Concatenation of 100 sequences yielded a perfect, noise-free power spectrum. (***b***) Same analysis as in (a) with addition of normally distributed noise. (***c***) Effect of phase shifts between concatenated sequences. (***c*-I**) Two sequences of 600 s and a periodicity of 60 s are concatenated with a 180° phase shift. (***c*-II**) Spectral decomposition of the signal in (c-I). The peak frequency localizes at 59 s; in parentheses: period calculated for two windows with no phase shift. (***c*-III**) and (***c*-IV**) Spectra calculated from 10 and 100 sequences. Similarly, the additional phase shifts between the sequences do not significantly deteriorate the recovery of the dominant frequency.

In Fig. S6*a-b*, we showed that concatenation of sufficient probing windows yield signals long enough for spectral analysis. However, this comes at the price of introducing a phase shift at the end of every period representing the time series from one probing window. Assembly and disassembly of different windows are not in synchrony. We tested the effect of phase shifts on the spectral analysis by adding random phase shifts in the range (0°…360°) between the concatenated signal pieces from different windows. An example with 180° phase shift is

displayed in Fig. S6 *c*I). To separate the effects of signal mixtures and noise from the one of the phase shifts, we limited this analysis to a single sine wave with period 60 s. Phase shifts appeared to minimally affect the frequency recovery even at the single-window level (Fig. S6 *c*II-IV).

In summary, Fig. S6 shows that the spectral analysis of assembly and disassembly maps requires integration of a large number of probing windows. Whereas our simulations were realistic in terms of the chosen frequencies and amplitude noise levels, we did not consider fluctuations in the periodicity of the sine wave mixtures over time. Such fluctuations occur due to data noise, but they could also reflect significant transients in the mechanism of F-actin turnover. One way to examine temporal variations in the frequency spectra would be by wavelet analysis. However, these methods were not robust in presence of the high noise level of our data and they lose their advantages over the Fourier Transform if applied with the same averaging strategy as described above. Our labs are currently working on developing better fluorescent probes and image acquisition systems to acquire longer movies with less noise. This will enable us to extend the spectral analyses towards the identification of temporal transients. At this point, we had to limit the analysis to the assumption of a stationary process. The relatively low noise floor of the experimental spectra and the small number of characteristic frequencies of remarkable stability between cells, despite the differences in flow (Fig. 4), suggested that this assumption was mostly valid for the time scales analyzed in this paper.

References

1. Ponti, A., P. Vallotton, W. C. Salmon, C. M. Waterman-Storer, and G. Danuser. 2003. Computational Analysis of F-Actin Turnover in Cortical Actin Meshworks Using Fluorescent Speckle Microscopy. Biophys. J. 84:3336-3352.

2. Inoue, S. and R. Oldenbourg. 1995. Microscopes. In Handbook of Optics. M. Bass, editor. 2nd ed. McGraw-Hill, Inc. New York.

3. Thomann, D., D. R. Rines, P. K. Sorger, and G. Danuser. 2002. Automatic fluorescent tag detection in 3D with super- resolution: application to the analysis of chromosome movement. J. Microsc.-Oxf. 208:49-64.

4. Ponti, A. 2004. High-Resolution Analysis of F-actin Meshwork Kinetics and Kinematics using Computational Fluorescent Speckle Microscopy. Zurich: ETH Zurich.